A Hybrid Multigroup/Continuous-Energy Monte Carlo Method for Solving the Boltzmann-Fokker-Planck Equation

J. E. Morel

Los Alamos National Laboratory, Los Alamos, New Mexico 87545

Leonard J. Lorence, Jr., Ronald P. Kensek, and John A. Halbleib
Sandia National Laboratories, Albuquerque, New Mexico 87185

and

D. P. Sloan

CH2M HILL, 599 Oak Ridge Turnpike, Oak Ridge, Tennessee 37830

Abstract—*A hybrid multigroup/continuous-energy Monte Carlo algorithm is developed for solving the Boltzmann-Fokker-Planck equation. This algorithm differs significantly from previous charged-particle Monte Carlo algorithms. Most importantly, it can be used to perform both forward and adjoint transport calculations, using the same basic multigroup cross-section data. The new algorithm is fully described, computationally tested, and compared with a standard condensed history algorithm for coupled electron-photon transport calculations.*

I. INTRODUCTION

Over the last several years, the Boltzmann-Fokker-Planck (BFP) equation has been applied to both neutral- and charged-particle transport problems.[1,2] The BFP equation uses the traditional Boltzmann integral operator together with differential Fokker-Planck operators to treat the scattering. Fokker-Planck operators are asymptotic approximations to the Boltzmann operator that apply in the forward-peaked scattering limit.[3] It is easier to numerically treat forward-peaked scattering and the small energy losses associated with such scattering using Fokker-Planck operators rather than the Boltzmann operator. In a BFP calculation, the forward-peaked or "singular" component of the scattering cross section is treated with the Fokker-Planck operator, and the large-angle or "smooth" component is treated with the Boltzmann operator.[4] Most of the

methods recently developed to solve the BFP equation have been deterministic.[1-3] A few Monte Carlo methods have been developed to solve the BFP equation for specific types of particles,[5,6] but we are unaware of any Monte Carlo methods for solving a general form of the BFP equation associated with both neutral and charged particles. This is to be contrasted with the standard multigroup Monte Carlo method,[7] which was developed to solve a general form of the Boltzmann equation associated with a wide variety of neutral particles.

The purpose of this study is to generalize the standard neutral-particle multigroup Monte Carlo method so that it can be used to perform BFP calculations as well as standard Boltzmann calculations. There are three main advantages to this approach. The first advantage is that it leads to a generalized Monte Carlo algorithm that can be used to perform transport calculations for a wide variety of both neutral and charged

particles, given appropriate multigroup cross-section data. The second advantage is that adjoint calculations can be performed using the same multigroup cross-section data used for forward calculations. The third advantage is that the adjoint algorithm is nearly identical to the forward algorithm. The difficulties associated with developing continuous-energy adjoint methods are well known[8] and exemplified by the absence of production continuous-energy Monte Carlo adjoint codes in both the neutral- and charged-particle transport communities.

The remainder of this paper is organized as follows. First, we describe the form of the BFP equation that our method solves. Then, we construct an approximate hybrid multigroup/continuous-energy representation for the BFP equation that is closely related to the standard multigroup approximation for the Boltzmann equation. Our forward Monte Carlo method solves this approximate BFP equation rather than the exact BFP equation in the same sense that the standard multigroup Monte Carlo method solves the multigroup Boltzmann equation rather than the exact Boltzmann equation. Next, we describe our forward Monte Carlo algorithm in detail. The adjoint of the approximate BFP equation is next discussed, followed by a description of the Monte Carlo techniques used to solve this adjoint equation. The techniques used to generate the BFP cross-section data required to perform coupled electron-photon transport calculations with our method are then discussed. Computational results are next given for coupled electron-photon transport problems, which compared both our forward and adjoint methods with a standard condensed history[5] forward Monte Carlo method. Finally, we give a summary and conclusions.

II. THE BOLTZMANN-FOKKER-PLANCK
EQUATION

The BFP equation that we approximately solve can be written as follows[1]:

$$
\mathbf{\Omega} \cdot \nabla \psi + \sigma_t \psi = \int_0^\infty \int_0^{2\pi} \int_{-1}^{+1} \sigma_s(E' \to E, \mu_0)
$$
$$
\times \psi(\mu', \phi', E') \, d\mu' \, d\phi' \, dE'
$$
$$
+ \frac{\alpha}{2} \left\{ \frac{\partial}{\partial \mu} \left[(1 - \mu^2) \frac{\partial \psi}{\partial \mu} \right] \right.
$$
$$
\left. + \frac{1}{1 - \mu^2} \frac{\partial^2 \psi}{\partial \phi^2} \right\}
$$
$$
+ \frac{\partial}{\partial E} [S\psi] + Q , \tag{1}
$$

where

$$
\mu_0 = \mu' \mu + [(1 - \mu'^2)(1 - \mu^2)]^{1/2} \cos(\phi' - \phi) , \tag{2}
$$

and where

ψ = angular flux

μ = cosine of the directional polar angle

ϕ = directional azimuthal angle

E = energy variable

σ_t = smooth-component total macroscopic cross section

σ_s = smooth-component macroscopic differential scattering cross section

α = restricted momentum transfer

S = restricted stopping power

Q = inhomogeneous source.

The last two operators in Eq. (1) are Fokker-Planck operators. The angular operator is known as the continuous-scattering operator, and the energy operator is known as the continuous slowing down operator. The continuous-scattering operator effectively causes particles to continuously scatter or diffuse in direction space in such a way that the mean change in direction cosine per unit path length is equal to the restricted momentum transfer. The continuous-slowing-down operator effectively causes particles to continuously lose energy in such a way that the mean energy loss per unit path length is equal to the restricted stopping power. These operators become asymptotically equivalent to the Boltzmann operator in the forward-peaked elastic scattering limit.[3] If the scattering is highly forward-peaked, it is easier to numerically treat these Fokker-Planck operators than the Boltzmann equation. The BFP equation is used when the scattering has both a forward-peaked component and a significant large-angle component. The Fokker-Planck operators are used to model the forward-peaked or singular component, and the Boltzmann operator is used to model the large-angle or smooth component. Thus, the cross sections appearing in Eq. (1) represent only the smooth component of the scattering, and the Fokker-Planck operators appearing in Eq. (1) represent only the singular component of the scattering. This is why the momentum transfer and stopping power are referred to as "restricted," i.e., restricted to the singular scattering component. More specifically, let $\sigma_{ss}(E' \to E, \mu_0)$ denote the singular or forward-peaked scattering cross section. Then,

$$
\alpha(E) = \int_0^E 2\pi \int_{-1}^{+1} \sigma_{ss}(E \to E', \mu_0)(1 - \mu_0) \, d\mu_0 \, dE ,
$$
$$
\tag{3}
$$

and

$$
S(E) = \int_0^E 2\pi \int_{-1}^{+1} \sigma_{ss}(E \to E', \mu_0)(E - E') \, d\mu_0 \, dE .
$$
$$
\tag{4}
$$

Equation (1) describes the transport of one type of particle at suprathermal energies. A second Fokker-Planck energy operator is required to treat particles at thermal energies.[3] We consider only suprathermal transport in this paper, but our method could easily be generalized to treat particles at thermal energies by using the multigroup approximation for the second-order Fokker-Planck operator described in Ref. 3. Although we derive our method for a single particle type, it is well known that a multigroup method can treat multiple particles simply by associating each group with both an energy interval and a particle type. Our multigroup BFP method retains this property.

III. THE APPROXIMATE BOLTZMANN-FOKKER-PLANCK EQUATION

In this section, we derive the approximate BFP equation associated with our Monte Carlo algorithm. This approximate equation is solved by our Monte Carlo algorithm in the same sense that the Boltzmann equation is solved by the standard multigroup Monte Carlo algorithm. To obtain this equation, we first replace the continuous-scattering operator with a certain type of Boltzmann-scattering operator. We next replace the smooth-component scattering cross sections with Legendre polynomial expansions of arbitrary but finite degree. Finally, we replace the energy dependence of the transport operator with a piecewise-constant approximation.

III.A. A Boltzmann Approximation to the Angular Fokker-Planck Operator

In this section, we take the first step in the development of our approximate BFP equation by replacing the angular Fokker-Planck operator of Eq. (1) with a Boltzmann operator. This replacement is made simply because it enables us to simulate the continuous-scattering process using a standard neutral-particle Monte Carlo algorithm. Specifically, the angular Fokker-Planck operator is replaced with the scattering operator B_α:

$$B_\alpha \psi = \int_0^{2\pi} \int_{-1}^{+1} \sigma_\alpha(E, \mu_0) \psi(\mu', \phi', E) \, d\mu' \, d\phi' - \sigma_\alpha \psi \ ,$$

(5)

where

$$\sigma_\alpha(E, \mu_0) = \frac{\alpha(E)}{1 - \mu_s} \frac{1}{2\pi} \delta(\mu_0 - \mu_s) \ ,$$

(6)

and where μ_s, which we refer to as the Fokker-Planck scattering angle, is a variable parameter. Note that there is no energy loss associated with B_α and further that there is only one polar angle of scatter. The cosine of this scattering angle is equal to μ_s. To avoid confusion between the smooth-component Boltzmann op-

erator appearing in Eq. (1) and B_α, we refer to all quantities associated with the smooth-component Boltzmann operator as "smooth-component" quantities and all quantities associated with B_α as "continuous-scattering" quantities. For instance, we refer to σ_α as the continuous-scattering cross section and to σ_t as the smooth-component total cross section.

We now demonstrate that B_α converges to the continuous-scattering operator in the limit as $\mu_s \to 1$. In particular, we show that any fixed number of eigenvalues and eigenfunctions of the continuous-scattering operator can be preserved to an arbitrary degree of accuracy as a function of μ_s. First, we define the spherical-harmonic function Y_l^m:

$$Y_l^m(\mu, \phi) = P_l^{|m|}(\mu) e^{im\phi} \ , \quad m = -l, l, \ l = 0, \infty \ , \quad (7)$$

where $P_l^m(\mu)$ is the associated Legendre function of degree l and order m. Expanding the scattering cross section in Eq. (5) in Legendre polynomials, applying the spherical-harmonics addition theorem, and then operating on the function Y_l^m, we find that

$$B_\alpha Y_l^m = [\sigma_\alpha^{(l)} - \sigma_\alpha^{(0)}] Y_l^m \ ,$$

(8)

where

$$\sigma_\alpha^{(0)} = \frac{\alpha}{1 - \mu_s}$$

(9)

and

$$\sigma_\alpha^{(l)} = \frac{\alpha}{1 - \mu_s} P_l(\mu_s) \ .$$

(10)

From Eq. (9), it follows that the spherical-harmonic functions are eigenfunctions of B_α.

The associated Legendre function P_l^m satisfies Legendre's associated differential equation[9]:

$$\frac{\partial}{\partial \mu} \left[(1 - \mu^2) \frac{\partial}{\partial \mu} P_l^m \right] + \left[l(l + 1) - \frac{m^2}{1 - \mu^2} \right] P_l^m = 0 \ .$$

(11)

Applying the Fokker-Planck angular operator to Y_l^m, and using Eq. (11), we find that

$$F_\alpha Y_l^m = -\frac{\alpha}{2} l(l + 1) Y_l^m \ ,$$

(12)

where

$$F_\alpha \psi = \frac{\alpha}{2} \left\{ \frac{\partial}{\partial \mu} \left[(1 - \mu^2) \frac{\partial \psi}{\partial \mu} \right] + \frac{1}{1 - \mu^2} \frac{\partial^2 \psi}{\partial \phi^2} \right\} \ . \quad (13)$$

It follows from Eq. (12) that the spherical-harmonic functions are eigenfunctions of the Fokker-Planck angular operator. Thus, the spherical-harmonics functions are eigenfunctions of both B_α and the angular Fokker-Planck operator.

To show that B_α becomes equivalent to F_α in the limit as $\mu_s \to 1$, we expand the eigenvalues of B_α in a first-order Taylor series about $\mu_s = 1$:

$$\sigma_\alpha^{(l)} - \sigma_\alpha^{(0)} = \frac{\alpha}{1 - \mu_s} \left[P_l(\mu_s) - 1 \right] \ ,$$

$$= \frac{\alpha}{1 - \mu_s} \left[P_l(1) + \frac{\partial}{\partial x} P_l(x) \Big|_{x=1} \right.$$

$$\left. \times (\mu_s - 1) - 1 \right] \ . \tag{14}$$

Since

$$P_l(1) = 1 \tag{15}$$

and

$$\frac{\partial}{\partial x} P_l(x) \Big|_{x=1} = \frac{l(l+1)}{2} \ , \tag{16}$$

Eq. (14) becomes

$$\sigma_\alpha^{(l)} - \sigma_\alpha^{(0)} = -\frac{\alpha}{2} l(l+1) \ . \tag{17}$$

Comparing Eqs. (8), (12), and (17), we find that the eigenvalues of B_α converge to the eigenvalues of F_α in the limit as $\mu_s \to 1$. Thus, these two operators become equivalent in this limit.

To impart some sense of the manner in which the eigenvalues of B_α approach those of F_α, the first 16 eigenvalues of B_α are compared with the eigenvalues of F_α in Table I for several values of μ_s with $\alpha = 1$. It can be seen from Table I that the first two eigenvalues are exact for every value of μ_s, but the higher order eigenvalues are approximate. The error in each eigenvalue

monotonically decreases as μ_s is increased, but for any fixed value of μ_s, the error monotonically increases with increasing eigenvalue index. Thus, while B_α does in fact converge to F_α as $\mu_s \to 1$, it does so nonuniformly. Thus, for any fixed value of μ_s, the high-order eigenvalues of F_α are grossly underestimated by B_α. Fortunately, this error in the high-order eigenvalues is usually unimportant. To explain why this is so, we first consider the following time-dependent transport equation:

$$\frac{\partial}{\partial t} \psi(t,\mu) = \frac{\alpha}{2} \frac{\partial}{\partial \mu} \left[(1 - \mu^2) \frac{\partial \psi}{\partial \mu} \right] \ , \tag{18}$$

with initial condition

$$\psi(0,\mu) = \frac{1}{2\pi} \delta(\mu - 1) \ . \tag{19}$$

The solution to Eq. (19) is

$$\psi = \frac{1}{2\pi} \sum_{l=0}^{\infty} \exp(-\lambda_l t) P_l(\mu) \ , \tag{20}$$

where λ_l is the eigenvalue of F_α with Legendre index l. Note from Eq. (20) that the l'th Legendre moment of the angular flux solution is exponentially attenuated in proportion to λ_l. Since these eigenvalues become unbounded for large l, it follows that the high-order flux moments will be "very small" for all nonzero values of t. A gross underestimate of λ_l will still result in a very small flux moment if the approximate eigenvalue is large relative to $1/t$. Thus, for sufficiently large times, an accurate solution can be obtained even though the high-order eigenvalues are grossly underestimated.

This example illustrates the following basic idea. In problems with highly forward-peaked scattering, the high-order flux moments are much more rapidly attenuated than the low-order moments as the particle distribution evolves in space and time. Thus, errors in the eigenvalues associated with the high-order moments are not serious as long as the approximate eigenvalues are large relative to the temporal and spatial scale lengths associated with a given problem.

All condensed history algorithms are limited to problems with spatial and temporal scale lengths that are large relative to a mean free path and the mean time between scattering events, respectively. Thus, a scale length restriction is to be expected for our algorithm.

III.B. Legendre Cross-Section Expansions

In this section, we expand the smooth-component scattering cross section in Legendre polynomials. This is appropriate since all standard multigroup cross-section data assume such an expansion:

$$\hat{\sigma}_s(E' \to E, \mu_0) = \sum_{l=0}^{L} \frac{2l+1}{4\pi} \sigma_s^{(l)}(E' \to E) P_l(\mu_0) \ , \tag{21}$$

TABLE I

Comparison of F_α and B_α Eigenvalues

Legendre Index	F_α	B_α		
		$\mu_s = 0.9$	$\mu_s = 0.95$	$\mu_s = 0.99$
0	0.0	0.00	0.00	0.00
1	1.0	1.00	1.00	1.00
2	3.0	2.85	2.93	2.98
3	6.0	5.28	5.63	5.93
4	10.0	7.92	8.92	9.78
5	15.0	10.41	12.55	14.48
6	21.0	12.41	16.25	19.97
7	28.0	13.68	19.78	26.16
8	36.0	14.01	22.88	32.96
9	45.0	13.70	25.37	40.28
10	55.0	12.63	27.10	47.99
11	66.0	11.16	27.99	56.00
12	78.0	9.59	28.05	64.18
13	91.0	8.22	27.32	72.42
14	105.0	7.29	25.94	80.61
15	120.0	6.95	24.08	88.62

where

$$\sigma_s^{(l)}(E' \to E) = 2\pi \int_{-1}^{+1} \sigma_s(E' \to E, \mu_0) P_l(\mu_0) \, d\mu_0 \, ,$$
$$l = 0, L \, , \qquad (22)$$

and where $P_l(\mu_0)$ denotes the Legendre polynomial of degree l, and L denotes the degree of the expansion. A circumflex is used in Eq. (21) to denote the approximate nature of the cross section. It is considered to be approximate because the Legendre expansion is finite. In Sec. III.C, we make further approximations to this cross section.

III.C. The Hybrid Multigroup/Continuous-Energy Approximation

In this section, we make an approximation in energy that yields a continuous-energy transport equation that is closely related to the multigroup transport equations. In particular, we use piecewise-constant weighting functions to obtain weighted least-squares fits in energy for the smooth-component cross sections, restricted momentum transfer, and restricted stopping power. We begin by partitioning the energy domain into N contiguous intervals or "groups." In analogy with the standard multigroup method, the highest energy group carries an index of 1, and the lowest energy group carries an index of N. Each group g has a minimum energy $E_{g+1/2}$ and a maximum energy $E_{g-1/2}$. The basis functions $[B_g(E)]_{g=1}^N$ are defined as

$$B_g(E) = 1.0 \, , \quad \text{for } E \in (E_{g+1/2}, E_{g-1/2}) \, ,$$
$$= 0.0 \, , \quad \text{otherwise} \, . \qquad (23)$$

Given a function $f(E)$, we obtain a fit to that function, $\tilde{f}(E)$, as

$$\tilde{f}(E) = \sum_{g=1}^N f_g B_g(E) \, , \qquad (24)$$

where the expansion coefficients $\{f_g\}_{g=1}^N$ are chosen to minimize the following functional:

$$\Gamma = \int_{E_{N+1/2}}^{E_{1/2}} [f(E) - \tilde{f}(E)]^2 W(E) \, dE \, , \qquad (25)$$

where $W(E)$ is an arbitrary weighting function. For convenience, we assume that

$$W(E) = \sum_{g=1}^N W_g(E) \, , \qquad (26)$$

where each $W_g(E)$ is zero for all energies outside of group g. We also assume that the integral of $W_g(E)$ over group g is ΔE_g, where $\Delta E_g = E_{g-1/2} - E_{g+1/2}$. Under these assumptions, the expansion coefficients take the following form:

$$f_g = \frac{1}{\Delta E_g} \int_{E_{g+1/2}}^{E_{g-1/2}} f(E) W_g(E) \, dE \, . \qquad (27)$$

In accordance with this procedure, we define the approximate smooth-component total cross section by

$$\tilde{\sigma}_t(E) = \sum_{g=1}^N \sigma_{t,g} B_g(E) \, , \qquad (28)$$

where

$$\sigma_{t,g} = \frac{1}{\Delta E_g} \int_{E_{g+1/2}}^{E_{g-1/2}} \sigma_t(E) W_g(E) \, dE \, ; \qquad (29)$$

the approximate smooth-component scattering cross section by

$$\tilde{\sigma}_s(E' \to E, \mu_0) = \sum_{k=1}^N \sum_{g=1}^N \sum_{l=0}^L \frac{2l+1}{4\pi}$$
$$\times \sigma_{s,k \to g}^{(l)} \mathcal{B}_{k,g}(E', E) P_l(\mu_0) \, , \qquad (30)$$

where

$$\sigma_{s,k \to g}^{(l)} = \frac{1}{\Delta E_k} \int_{E_{g+1/2}}^{E_{g-1/2}} \int_{E_{k+1/2}}^{E_{k-1/2}} \sigma_s^l(E' \to E)$$
$$\times W_k(E') W_g(E) \, dE' \, dE \, , \qquad (31)$$

and

$$\mathcal{B}_{k,g}(E', E) = \frac{B_k(E') B_g(E)}{\Delta E_g} \, ; \qquad (32)$$

the approximate restricted momentum transfer by

$$\tilde{\alpha}(E) = \sum_{g=1}^N \alpha_g B_g(E) \, , \qquad (33)$$

where

$$\alpha_g = \frac{1}{\Delta E_g} \int_{E_{g+1/2}}^{E_{g-1/2}} \alpha(E) W_g(E) \, dE \, ; \qquad (34)$$

and the approximate restricted stopping power by

$$\tilde{S}(E) = \sum_{g=1}^N S_g B_g(E) \, , \qquad (35)$$

where

$$S_g = \frac{1}{\Delta E_g} \int_{E_{g+1/2}}^{E_{g-1/2}} S(E) W_g(E) \, dE \, . \qquad (36)$$

Note that Eqs. (33) and (6) imply that $\sigma_\alpha(E, \mu_0)$ is replaced with $\tilde{\sigma}_\alpha(E, \mu_0)$, where

$$\tilde{\sigma}_\alpha(E, \mu_0) = \frac{\tilde{\alpha}(E)}{1 - \mu_s} \frac{1}{2\pi} \delta(\mu_0 - \mu_s) \, . \qquad (37)$$

Also note that the use of Eq. (32) makes it possible for upscatter to occur when $k = g$ even though there is no upscatter in the problem. Most importantly, we have found that this upscatter can lead to excessive energy

straggling. This problem is avoided using the following definition in place of Eq. (32) for the $k = g$ case:

$$\mathcal{B}_{g,g}(E',E) = \delta(E' - E)B_g(E) . \tag{38}$$

Note that use of the expression in Eq. (38) ensures that within-group scattering leaves the particle energy unchanged. This is in accordance with the standard multigroup method.

Taking all of the approximations that we have made into account, we can write our final approximate BFP equation as

$$
\begin{aligned}
\mathbf{\Omega} \cdot \nabla \psi + \tilde{\sigma}_t \psi &= \int_E^{E_{1/2}} \int_0^{2\pi} \int_{-1}^{+1} \tilde{\sigma}_s(E' \rightarrow E, \mu_0) \\
&\quad \times \psi(\mu', \phi', E') \, d\mu' \, d\phi' \, dE' \\
&\quad + \int_0^{2\pi} \int_{-1}^{+1} \tilde{\sigma}_\alpha(\mu_0) \psi(\mu', \phi') \, d\mu' \, d\phi' \\
&\quad - \tilde{\sigma}_\alpha \psi + \frac{\partial}{\partial E} [\tilde{S}\psi] + Q ,
\end{aligned}
\tag{39}
$$

where $\tilde{\sigma}_t$ is defined by Eqs. (28) and (29); $\tilde{\sigma}_s(E' \rightarrow E, \mu_0)$ is defined by Eqs. (30) and (31); $\tilde{\sigma}_\alpha(\mu_0)$ is defined by Eqs. (33), (34), and (37); $\tilde{\sigma}_\alpha$ is the integral over all directions of $\tilde{\sigma}_\alpha(\mu_0)$; and $\tilde{S}$ is defined by Eqs. (35) and (36).

Note from Eqs. (29) and (31), respectively, that the expansion coefficients that we have defined for the total smooth-component cross section and the smooth-component scattering kernel, $\sigma_{t,g}$ and $\sigma_{k \rightarrow g}^{(l)}$, respectively, are identical to the standard multigroup-Legendre coefficients for these functions.[10] Under certain conditions, this identity makes our method equivalent to the standard multigroup method. To demonstrate this, we first write Eq. (39) with the Fokker-Planck terms set to zero:

$$
\begin{aligned}
\mathbf{\Omega} \cdot \nabla \psi + \tilde{\sigma}_t \psi &= \int_0^\infty \int_0^{2\pi} \int_{-1}^{+1} \tilde{\sigma}_s(E' \rightarrow E, \mu_0) \\
&\quad \times \psi(\mu', \phi', E') \, d\mu' \, d\phi' \, dE' + Q .
\end{aligned}
\tag{40}
$$

Successively integrating Eq. (40) over each energy group, we obtain the following set of equations:

$$
\begin{aligned}
&\mathbf{\Omega} \cdot \nabla \psi_g + \tilde{\sigma}_{t,g} \psi_g \\
&= \int_0^{2\pi} \int_{-1}^{+1} \sum_{k=1}^{g} \sum_{l=0}^{L} \frac{2l+1}{4\pi} \sigma_{k \rightarrow g}^{(l)} P_l(\mu_0) \\
&\quad \times \psi_k(\mu', \phi') \, d\mu' \, d\phi' + Q_g , \quad g = 1, G ,
\end{aligned}
\tag{41}
$$

where

$$\psi_g = \int_{E_{g+1/2}}^{E_{g-1/2}} \psi(E) \, dE \tag{42}$$

and

$$Q_g = \int_{E_{g+1/2}}^{E_{g-1/2}} Q(E) \, dE . \tag{43}$$

Equation (41) is the standard multigroup Boltzmann equation. Thus, if our hybrid multigroup/continuous-energy approximation is applied only to the Boltzmann equation, it yields group-integrated fluxes that are identical to those obtained with the standard multigroup method. It is for this reason that we consider our technique to be a direct generalization of that method.

Energetic charged particles generally undergo an extremely large number of highly forward-peaked scattering events before slowing down to thermal energies. Thus, one usually cannot afford to simulate each individual charged-particle collision in a Monte Carlo algorithm. So-called "condensed history" algorithms have been developed to deal with this fundamental difficulty.[5] In such algorithms, the energy and direction of a particle is changed after each "condensed collision" to approximate the cumulative effect of the many real small-angle collisions that would have actually occurred between these condensed collisions. Furthermore, the particles travel a fixed distance between condensed collisions.[a] The algorithm that we have developed is a form of condensed history algorithm, but it fundamentally differs from standard condensed history algorithms in that there is an exponential distribution of path lengths between collisions rather than a fixed path length. This exponential path length distribution arises from the use of the Boltzmann operator B_α in place of the angular Fokker-Planck operator F_α. Thus, our algorithm is much more similar to a neutral-particle Monte Carlo algorithm than the standard condensed history algorithm. The accuracy of the transport solution that we obtain depends on the number of energy groups, the order of the Legendre cross-section expansion, and the value of the parameter μ_s. In the limit as the number of groups and the Legendre expansion order become arbitrarily large, and μ_s approaches unity, our approximate BFP equation, Eq. (39), becomes equivalent to the exact BFP equation, Eq. (1).

IV. SOLUTION OF THE APPROXIMATE BOLTZMANN-FOKKER-PLANCK EQUATION

In this section, we describe the Monte Carlo method used to solve Eq. (39). In Sec. IV.A, we describe the use of discrete angular distributions for the smooth-component Boltzmann-scattering distributions to eliminate difficulties arising from the nonpositive character of highly truncated Legendre cross-section expansions. In Sec. IV.B, we describe our basic BFP Monte Carlo algorithm in detail.

---

[a]Not all collisions are condensed in condensed history codes. In particular, so-called "catastrophic" collisions (large-angle or large energy-loss collisions) are treated in the usual manner and hence have exponential path length distributions.

IV.A. Smooth-Component Scattering Angles

Because of the anisotropy of the scattering, charged-particle transport calculations must generally be carried out with highly truncated cross-section expansions. Surprisingly, this in itself does not preclude an accurate solution. For instance, let us assume that the angular flux for a given problem can be exactly represented by a spherical-harmonic expansion of degree L. This solution must exactly satisfy the P_L equations.[10] Since only the cross-section moments of degree l, where $l \leq L$, appear in the P_L equations, it follows that a truncated cross-section expansion of degree L will yield the same solution as a converged expansion of higher order. Thus, if the exact angular flux for a given problem can be accurately represented with a spherical-harmonic expansion of degree L, one can expect an accurate solution using a cross-section expansion of similar degree whether or not it is truncated.

Truncated cross-section expansions often have negative values at certain values of the scattering angle. Although these negativities do not necessarily affect accuracy, they do cause certain Monte Carlo particles to assume negative weights. A combination of negative and positive weights often leads to large statistical errors. Thus, sampling from truncated cross-section expansions is undesirable. This problem can be overcome by means of generalized Gauss quadratures.[11] Such quadratures are used in the MORSE multigroup Monte Carlo code to construct discrete-scattering distributions.[7] The derivation of generalized Gauss quadratures and their implementation in the MORSE code are discussed in Ref. 7.

A generalized Gauss quadrature is defined as follows. Given a weight function $W(\mu)$ defined over $[-1,+1]$, find a set of M cosines and weights, $\{\mu_m, w_m\}_{m=1}^{M}$, such that

$$\sum_{m=1}^{M} f(\mu_m) w_m = 2\pi \int_{-1}^{+1} f(\mu) W(\mu) \, d\mu , \qquad (44)$$

where $f(\mu)$ is any polynomial of degree $2M - 1$ or less. It can be shown that if $W(\mu)$ is positive for all $\mu \in (-1,+1)$, the discrete cosines must lie on the interval $(-1,+1)$, and the weights must be positive. To demonstrate the utility of these quadratures in Monte Carlo calculations, we first assume that the weight function is in fact a differential-scattering cross section, $\sigma_s(\mu_0)$. It follows from Eq. (44) that the Legendre moments of this cross section are exactly given through degree $2M - 1$ by

$$\sigma^{(l)} = \sum_{m=1}^{M} P_l(\mu_m) w_m . \qquad (45)$$

It is easily shown that the following discrete cross section has these same moments through degree $2M - 1$:

$$\sigma_d(\mu_0) = \frac{1}{2\pi} \sum_{m=1}^{M} \delta(\mu_0 - \mu_m) w_m . \qquad (46)$$

In particular, multiplying Eq. (46) by $P_l(\mu_0)$ and integrating over all directions, we obtain

$$\sigma_d^{(l)} = \sum_{m=1}^{M} P_l(\mu_m) w_m . \qquad (47)$$

Since all cross sections are strictly positive functions, the quadrature cosines must lie on $(-1,+1)$, and the weights must be positive. Thus, the discrete cross section defined by Eq. (46) is physically acceptable and will not generate Monte Carlo particles with negative weights. Most importantly, the discrete cross section has the same Legendre moments as the exact cross section through degree $2M - 1$. Therefore, the discrete cross section, the truncated cross-section expansion of degree $2M - 1$, and the exact cross section produce the same spherical-harmonic solution of degree $2M - 1$. If the exact solution to a given problem can be accurately approximated with a spherical-harmonic expansion of degree $2M - 1$, it follows that the discrete cross section can be substituted for either the truncated cross-section expansion or the exact cross section without a significant loss of accuracy in the solution. This is the theoretical basis for using the discrete cross sections in a Monte Carlo algorithm.

The Gauss quadrature set is directly constructed in terms of the cross-section moments through degree $2M - 1$. Given a set of moments, physically acceptable cosines and weights must be obtained whenever there exists a strictly positive function on $[-1,+1]$ that has the same moments. If any one of the quadrature cosines lies outside of $(-1,+1)$, or if any one of the quadrature weights is negative, one can conclude that an error was made in calculating the cross-section moments. Thus, one can use the Gauss quadrature technique to detect erroneous cross-section data.

For reasons explained later, we use Radau quadratures rather than Gauss quadratures to generate discrete-scattering cross sections. The two quadratures are quite similar, except that a Radau set always has a cosine at $\mu = 1$. In particular, a Radau quadrature is defined as follows. Given a weight function $W(\mu)$ defined over $[-1,+1]$, and given that $\mu_1 = 1$, find a set of $M - 1$ cosines and M weights such that

$$\sum_{m=1}^{M} f(\mu_m) w_m = 2\pi \int_{-1}^{+1} f(\mu) W(\mu) \, d\mu , \qquad (48)$$

where $f(\mu)$ is any polynomial of degree $2M - 2$ or less. It can be shown that if $W(\mu)$ is positive for all $\mu \in (-1,+1)$, the discrete cosines must lie on the interval $(-1,+1]$, and the weights must be positive. The Radau set has one less degree of accuracy than the Gauss set because one degree of freedom was lost by explicitly defining one of the cosines. A discrete-scattering cross section constructed from an M-point Radau set preserves $2M - 2$ moments of the exact cross section, and takes the following form:

$$\sigma_d(\mu_0) = \frac{1}{2\pi} \delta(\mu_0 - 1) w_1 + \frac{1}{2\pi} \sum_{m=2}^{M} \delta(\mu_0 - \mu_m) w_m \ . \tag{49}$$

For our application, Radau quadratures have an important advantage relative to Gauss quadratures. In particular, Radau quadratures give us a mechanism to significantly reduce (and thus "condense") charged-particle cross sections. In particular, given a discrete within-group Radau cross section, one can eliminate the straight-ahead component of the cross section without affecting the solution. This follows from the fact that straight-ahead scattering without an energy loss is equivalent to no scattering at all. The modified discrete cross section, which we refer to as the "Radau-condensed" cross section, is given by

$$\sigma_{rc}(\mu_0) = \frac{1}{2\pi} \sum_{m=2}^{M} \delta(\mu_0 - \mu_m) w_m \ . \tag{50}$$

If the scattering is highly forward-peaked, the total scattering cross section will be dramatically reduced. For instance, the ratio of the exact total scattering cross section to the condensed total scattering section, which we refer to as the condensation factor, is given by

$$C_f = \sigma_s^{(0)} / \sigma_{rc}^{(0)} = \frac{\sum_{m=1}^{M} w_m}{\sum_{m=2}^{M} w_m} \ . \tag{51}$$

Condensation factors are given in Table II for seven-point Radau quadratures generated with P_{12} cross-section expansions for electrons at several different energies in aluminum. Note that these electron cross sections are not smooth-component cross sections, but rather are complete cross sections that include both highly forward-peaked and large-angle scattering components. For 1-MeV electrons, the condensation factor is ~45. The condensation factor decreases with increasing quadrature order, or equivalently, increasing Legendre expansion degree. In the limit of an infinite quadrature order, the factor approaches unity. Thus, there is no cross-section condensation in this limit. If one chooses not to use the Fokker-Planck approximation for the singular component of the scattering, the use of Radau-condensed cross sections is

essential to achieve good efficiency in charged-particle transport calculations. We stress that accuracy is not compromised by using Radau-condensed cross sections provided that the exact angular flux solution can be well represented by a spherical-harmonic expansion of degree $2M - 2$. Our experience indicates that the use of the Fokker-Planck approximation for the singular component of the scattering in conjunction with Radau-condensed cross sections for the smooth component of the scattering results in somewhat greater computational efficiency than the use of Radau-condensed cross sections for both components. However, if cross-section decomposition techniques are difficult or expensive to apply, one can always obtain acceptable efficiency and accuracy using Radau-condensed cross sections for both scattering components.

It is easily shown that the Legendre moments of the Radau-condensed cross section take the following form:

$$\sigma_{rc}^{(l)} = \sigma_s^{(l)} - w_1 \ , \quad l = 0, 2M - 2 \ . \tag{52}$$

The extended transport correction technique[12,13] is nearly identical to our condensation technique. In particular, if we apply the standard extended transport correction to an expansion of degree $2M - 2$, we obtain the following transport-corrected (tc) moments:

$$\sigma_{tc}^{(l)} = \sigma_s^{(l)} - \sigma_s^{(2M-2)} \ , \quad l = 0, 2M - 2 \ . \tag{53}$$

Comparing Eqs. (52) and (53) we find that the two techniques differ only with respect to the constant subtracted from the exact cross-section moments. This constant represents the magnitude of the straight-ahead component of the truncated scattering cross-section expansion. The extended transport correction is based on the heuristic assumption that this straight-ahead component has a magnitude equal to the last moment of the expansion, whereas this magnitude is exactly calculated with the Radau quadrature technique. Not surprisingly, we have found that the extended transport correction method often yields a set of nonphysical condensed cross-section moments that are unsuitable for generating a discrete-scattering cross section. This occurs when (and only when) the condensation factor generated with the transport correction method exceeds that generated with the Radau condensation technique. For instance, in Table III we give condensation factors obtained with

TABLE II

Radau Condensation Factors

Electron Energy (MeV)	$\sigma_s^{(0)}/\sigma_{rc}^{(0)}$
0.01	2.04
0.10	7.09
1.00	45.5

TABLE III

Transport Correction Condensation Factors

Electron Energy (MeV)	$\sigma_s^{(0)}/\sigma_{tc}^{(0)}$
0.01	1.53
0.10	7.58
1.00	76.9

the extended transport correction method. Comparing Tables II and III, we find that the extended transport correction method yields nonphysical condensed cross-section moments for both the 1.0- and 0.1-MeV cases. Although the transport-condensed moments are physically acceptable for the 0.01-MeV case, they are undesirable relative to the Radau-condensed moments because the transport correction condensation factor is smaller than the Radau condensation factor and thus results in a less efficient Monte Carlo simulation.

An approximation is often made in electron transport that leads to multigroup cross sections of the following form:

$$\sigma_{g \to k}(\mu_0) = \sigma_{g \to k} \frac{1}{2\pi} \delta(\mu_0 - 1) , \qquad (54)$$

where $g \neq k$. A quadrature set corresponding to any such cross section must clearly have only one direction, and that direction must be $\mu = 1$. As one would suspect, singularities arise in the standard Radau (and Gauss) quadrature generation algorithms with a cross section of this form. Thus, we have modified the Radau algorithm to first explicitly check for a cross section of this form, and when one is found, to generate an appropriate one-point quadrature set.

The algorithms for constructing generalized Gauss and Radau quadratures are described in complete detail in Ref. 11.

IV.B. The Basic Boltzmann-Fokker-Planck Monte Carlo Algorithm

The Monte Carlo algorithm for solving our approximate BFP equation is very similar to that for solving the standard multigroup Boltzmann equation. The only significant differences between the algorithms arise from the presence of the continuous slowing down term in the BFP equation and our use of a hybrid multigroup/continuous-energy approximation for both the smooth-component Boltzmann kernel and the continuous-scattering Boltzmann kernel. The main effect of the continuous slowing down term is to continuously slow down particles as they travel between smooth-component Boltzmann and continuous-scattering Boltzmann collisions. An exact treatment of this term requires a continuous-energy Monte Carlo treatment. It is for this reason that we developed a hybrid multigroup/continuous-energy treatment. While pure multigroup Monte Carlo treatments have been developed for the continuous slowing down operator, they are accurate only when the flux varies slowly with energy.[14]

Since most of our BFP algorithm is based on standard Monte Carlo techniques, we do not describe it in full, but rather consider only its unique aspects. These aspects are confined to the particle collision algorithm, which we will now describe in detail. In the discussion that follows, the reader is assumed to be familiar with basic Monte Carlo techniques.[15]

We begin the description of our collision algorithm by considering a particle with energy, E_p, which lies within group g. Since our cross sections are constant for all energies within a group, the total collision cross section for this particle is given by the sum of the total smooth-component Boltzmann and continuous-scattering cross sections for group g:

$$\sigma_g^{total} = \sigma_{t,g} + \sigma_{\alpha,g} , \qquad (55)$$

where in accordance with Eqs. (33), (34), and (37)

$$\sigma_{\alpha,g} = \frac{\alpha_g}{1 - \mu_s} . \qquad (56)$$

The first step in the collision algorithm is to use σ_g^{total} to randomly sample a distance-to-collision, which we denote by D_c. This quantity simply represents distance that the particle will travel before experiencing a collision. The next step in the algorithm is to determine if the distance-to-collision that has been sampled is valid. This is done by calculating a quantity known as the distance-to-material boundary, which we denote by D_m. This quantity represents the maximum distance that the particle can travel before reaching a material interface. If the distance-to-collision exceeds the distance-to-material boundary, the cross section will change before the particle reaches the collision site, thereby invalidating the distance-to-collision originally sampled. When this occurs, the particle is first moved along its original trajectory a distance equal to the distance-to-material boundary. Next, its material index is changed to reflect the fact that it is now in a new material. Finally, a new distance-to-collision is sampled.

In our BFP algorithm, we must calculate not only the distance-to-material boundary but also a quantity called the distance-to-energy boundary, which we denote by D_e. The distance-to-energy boundary represents the distance that a particle in group g will travel before slowing down into group $g + 1$. In particular, since the restricted stopping power is constant within each group, the distance-to-energy boundary for a particle in group g is given by

$$D_e = \frac{E_p - E_{g+1/2}}{S_g} . \qquad (57)$$

If the distance-to-collision éxceeds the distance-to-energy boundary, the cross section will change before the particle reaches the collision site, thereby invalidating the distance-to-collision originally sampled. In response to this occurrence, we move the particle along its original trajectory a distance equal to the distance-to-energy boundary, give it a new energy equal to $E_{g+1/2}$, change the energy index of the particle to $g + 1$, and then sample a new distance-to-collision.

When a valid distance-to-collision is sampled, the particle is moved to the collision site. Its energy is then changed to reflect the energy lost through the action of

the continuous slowing down term while traveling to that collision site. Specifically,

$$E_p^{new} = E_p^{old} - S_g D_c .$$ (58)

Next, a random sampling is made to determine whether a smooth-component Boltzmann or continuous-scattering collision has occurred. The relevant probabilities for each event, $\mathcal{P}_B$ and $\mathcal{P}_\alpha$, are respectively given by

$$\mathcal{P}_B = \frac{\sigma_{t,g}}{\sigma_g^{total}} ,$$ (59)

and

$$\mathcal{P}_\alpha = \frac{\sigma_{\alpha,g}}{\sigma_g^{total}} .$$ (60)

If a continuous-scattering collision occurs, a new direction for the particle is randomly sampled based on a polar scattering angle with cosine equal to μ_s. The azimuthal scattering angle is randomly chosen with uniform probability on the interval $[0,2\pi]$. The collision generation process is then begun anew by sampling another distance-to-collision.

If a smooth-component Boltzmann collision occurs, the incident particle is considered to have been "removed," and the scattered or secondary particles that will emerge from the collision must be created at the collision site. The first step in this process is to sample the number of particles that will emerge from the collision. To sample this number, one must calculate the average number of particles that must emerge from the collision. This average, denoted by $\mathcal{M}$, is called the multiplicity factor, and it is defined for an incident particle in group g by

$$\mathcal{M} = \frac{1}{\sigma_{t,g}} \int_{E_{N+1/2}}^{E_{g-1/2}} \tilde{\sigma}_s^{(0)}(E_p \to E') \, dE' ,$$

$$= \frac{1}{\sigma_{t,g}} \sum_{k=g}^{N} \sigma_{s,g \to k}^{(0)} .$$ (61)

Any procedure for choosing the number of particles emerging from a collision will be valid as long as the average number emerging equals $\mathcal{M}$. The method that we use is quite simple. Specifically, given that $\mathcal{M} = I + R$, where I is an integer and R is a positive real number < 1.0, we choose to have either I or $I + 1$ particles emerge with probabilities of $1.0 - R$ and R, respectively. For example, let us assume that $\mathcal{M} = 2.4$. We choose either two emerging particles with probability 0.6 or three emerging particles with probability 0.4. This gives us the desired average of $2 \times 0.6 + 3 \times 0.4 = 2.4$.

The probability of generating a particle in group k from a collision in group g is given by

$$\mathcal{P}_{g \to k} = \frac{\int_{E_{k+1/2}}^{E_{k-1/2}} \tilde{\sigma}_s^{(0)}(E_p \to E') \, dE'}{\int_{E_{N+1/2}}^{E_{g-1/2}} \tilde{\sigma}_s^{(0)}(E_p \to E') \, dE'} ,$$

$$= \frac{\sigma_{s,g \to k}^{(0)}}{\sum_{j=g}^{N} \sigma_{s,g \to j}^{(0)}} .$$ (62)

For the case of within-group scattering, the energy of the scattered particle remains at exactly that of the incident particle. This is consistent with the delta-function dependence of the scattering kernel given in Eq. (38). For all other cases, a particle generated in group k from a collision in group g is given an energy randomly distributed with uniform probability between $E_{k-1/2}$ and $E_{k+1/2}$. This distribution of energies within a group is consistent with the piecewise-constant dependence of the scattering kernel given in Eq. (32).

The sampling of directions for the emerging particles is based on the discrete Radau distributions. These distributions yield the polar cosine of the emerging particle in the scattering frame of reference. The azimuthal angle in this frame is randomly sampled with uniform probability on the interval $[0,2\pi]$. A separate Radau distribution exists for each smooth-component Boltzmann group-to-group transfer.

Once the energy and direction for each of the emerging particles has been calculated, these particles are put in a "bank" since only one particle at a time can be tracked. The collision generation process is then begun anew by sampling a distance-to-collision for the next particle available from the bank.

V. THE ADJOINT BOLTZMANN-FOKKER-PLANCK EQUATION

The approximate adjoint BFP equation that we solve is the exact adjoint of the approximate forward BFP equation, Eq. (39). This ensures that adjoint and forward solutions for the same response will be identical in the absence of statistical error. This adjoint equation can be expressed as

$$-\mathbf{\Omega} \cdot \nabla \psi^\dagger + \tilde{\sigma}_t \psi^\dagger$$

$$= \int_{E_{N+1/2}}^{E} \int_0^{2\pi} \int_{-1}^{+1} \tilde{\sigma}_s(E \to E', \mu_0)$$

$$\times \psi^\dagger(r,\mu',\phi',E') \, d\mu' \, d\phi' \, dE'$$

$$+ \int_0^{2\pi} \int_{-1}^{+1} \sigma_\alpha(\mu_0)\psi^\dagger(\mu',\phi') \, d\mu' \, d\phi' - \sigma_\alpha \psi^\dagger$$

$$- \frac{\partial}{\partial E} [\tilde{S}\psi^\dagger] + \frac{\partial S}{\partial E} \psi^\dagger + Q^\dagger ,$$ (63)

where $\psi^\dagger$ denotes the adjoint angular flux and $Q^\dagger$ denotes the adjoint inhomogeneous source. Equation (63) is consistent with the standard definition for the inner product of two analytic phase-space functions, f and h (Ref. 10):

$$\langle f, h \rangle = \int\int\int fh \, dV \, d\Omega \, dE \ . \tag{64}$$

We previously demonstrated that if the Fokker-Planck terms are set to zero, our approximate forward BFP equation is equivalent to the standard Boltzmann multigroup equation. Such an equivalence does not formally exist for our approximate adjoint equation. This lack of equivalence arises from the fact that the inner product used to define the adjoint Boltzmann multigroup operator is not equivalent to the inner product defined by Eq. (64). In particular, the standard inner product for the multigroup method (neglecting space and direction variables) is the dot product:

$$[f, h] = \sum_{g=1}^{N} f_g h_g \ , \tag{65}$$

where

$$f_g = \int_{E_{g+1/2}}^{E_{g-1/2}} f(E) \, dE \ , \tag{66}$$

and

$$h_g = \int_{E_{g+1/2}}^{E_{g-1/2}} h(E) \, dE \ . \tag{67}$$

Re-expressing Eqs. (66) and (67) in terms of $f(\overline{E}_g)$ and $h(\overline{E}_g)$, the group-averaged values of $f(E)$ and $h(E)$, respectively, we get

$$f_g = f(\overline{E}_g)\Delta E_g \ , \tag{68}$$

and

$$h_g = h(\overline{E}_g)\Delta E_g \ . \tag{69}$$

Substituting Eqs. (68) and (69) into Eq. (65), we obtain

$$[f, h] = \sum_{g=1}^{N} f(\overline{E}_g) h(\overline{E}_g) \Delta E_g \Delta E_g \ . \tag{70}$$

The following relationship must hold in the limit as $\Delta E_g \to 0$ in order for Eq. (70) to be consistent with Eq. (64):

$$[f, h] = \sum_{g=1}^{N} \int_{E_{g+1/2}}^{E_{g-1/2}} f(E) h(E) \, dE \ . \tag{71}$$

Comparing Eqs. (70) and (71), we find that there is an extra ΔE_g in Eq. (70) that prevents consistency.

Fortunately, this lack of consistency has no practical significance because any valid inner product can be used to define the adjoint operator. Given a desired response, a valid inner product, and an associated adjoint equation, there exists an adjoint source function

that yields that desired response. One must simply take care to use the consistent inner product when calculating the adjoint source. For instance, a Boltzmann multigroup adjoint equation can be made consistent with the standard analytic inner product by defining the multigroup inner product as

$$[f, h] = \sum_{g=1}^{N} f_g h_g \frac{1}{\Delta E_g} \ . \tag{72}$$

The multigroup adjoint scattering matrix elements consistent with Eq. (72) are defined in terms of the forward elements as

$$\sigma_{s,k \to g}^{\dagger(l)} = \sigma_{s,g \to k}^{(l)} \frac{\Delta E_g}{\Delta E_k} \ , \tag{73}$$

whereas the adjoint multigroup elements consistent with Eq. (65) are obtained simply by transposing the forward matrix:

$$\sigma_{s,k \to g}^{\dagger(l)} = \sigma_{s,g \to k}^{(l)} \ . \tag{74}$$

Equations (73) and (74) are derived from the standard expression relating forward and adjoint matrices[16]:

$$\langle \mathbf{A}f, h \rangle = \langle f, \mathbf{A}^\dagger h \rangle \ , \tag{75}$$

where $\mathbf{A}$ is any matrix, and f and h are any two vectors.

Let us assume that the desired response $\Re$ is the energy-integrated scalar flux at the spatial point r_0:

$$\Re = \sum_{g=1}^{N} \left[\int\int \delta(r - r_0)\psi_g \, dV \, d\Omega \right] \ . \tag{76}$$

The multigroup adjoint source corresponding to Eq. (65) is

$$Q_g^\dagger = \delta(r - r_0) \ , \tag{77}$$

while the multigroup adjoint source corresponding to Eq. (72) is

$$Q_g^\dagger = \delta(r - r_0)\Delta E_g \ . \tag{78}$$

Equations (77) and (78) are derived from the standard expression relating the desired response and the adjoint source function[17]:

$$\Re = \langle \psi, Q^\dagger \rangle \ . \tag{79}$$

We stress that our approximate adjoint BFP equation will yield the same solution for a given response (neglecting statistical error), as our approximate forward BFP equation. Our adjoint equation, with the Fokker-Planck terms set to zero, is functionally equivalent to the standard adjoint Boltzmann multigroup equation because both equations will yield the same solution for a given response (neglecting statistical error). However, our BFP adjoint equation, with the Fokker-Planck terms set to zero, is not mathematically equivalent to the standard adjoint Boltzmann multigroup equation because different adjoint sources must be used in each equation to calculate the same response. The need for different adjoint sources arises from the fact

that each equation is consistent with a different inner product.

VI. SOLUTION OF THE ADJOINT BOLTZMANN-FOKKER-PLANCK EQUATION

The Monte Carlo solution of our approximate adjoint BFP equation is nearly identical to the solution of our approximate forward BFP equation. The only significant differences arise due to the effect of the adjoint continuous slowing down term. Let us first consider the similarities. Following the procedure used in standard multigroup Monte Carlo, the negative sign of the adjoint gradient operator is ignored while generating adjoint particle histories. Its presence need only be taken into account when one interprets the solution. In particular, the Monte Carlo solution for $\psi^\dagger(\Omega)$ must be interpreted as the solution for $\psi^\dagger(-\Omega)$. This is mathematically equivalent to the following technique. First, make the following definition:

$$\xi^\dagger(\Omega) = \psi^\dagger(-\Omega) \ . \tag{80}$$

Then, substitute $\xi^\dagger$ for $\psi^\dagger$ in Eq. (63), and solve for $\xi^\dagger$. One finds that the equation for $\xi^\dagger$ is the same as Eq. (63) except that the gradient operator has no negative sign.

The adjoint sampling of the distance-to-collision, distance-to-material boundary, collision type, and angular Fokker-Planck (continuous-scattering) scattering angle are identical because the approximate removal and continuous-scattering operators are self-adjoint. The adjoint sampling of the smooth-component Boltzmann scattering is functionally identical to the forward sampling because the adjoint approximate kernel has the same mathematical form as the forward approximate kernel. In particular, from Eq. (63) we find that the adjoint kernel can be expressed in terms of the forward kernel as

$$\tilde{\sigma}_s^\dagger(E' \to E, \mu_0) = \tilde{\sigma}_s(E \to E', \mu_0) \ . \tag{81}$$

Substituting from Eqs. (30), (32), and (38) into Eq. (81), we obtain

$$\tilde{\sigma}_s^{\dagger(l)}(E \to E') = \sum_{k=1}^{N} \sum_{g=1}^{N} \sigma_{s,k \to g}^{(l)} \circledB_{k,g}(E, E') \ ,$$

$$= \sum_{k=1}^{N} \sum_{g \ne k} \sigma_{s,k \to g}^{(l)} \frac{B_k(E) B_g(E')}{\Delta E_g}$$
$$+ \sigma_{s,k \to k}^{(l)} \delta(E - E') B_k(E') \ ,$$

$$= \sum_{k=1}^{N} \sum_{g \ne k} \sigma_{s,g \to k}^{(l)} \frac{B_g(E) B_k(E')}{\Delta E_k}$$
$$+ \sigma_{s,k \to k}^{(l)} \delta(E - E') B_k(E') \ ,$$

$$= \sum_{k=1}^{N} \sum_{g \ne k} \sigma_{s,g \to k}^{(l)} \frac{\Delta E_g}{\Delta E_k} \frac{B_k(E') B_g(E)}{\Delta E_g}$$
$$+ \sigma_{s,k \to k}^{(l)} \delta(E - E') B_k(E') \ , \tag{82}$$

$$= \sum_{k=1}^{N} \sum_{g \ne k} \sigma_{s,g \to k}^{(l)} \frac{\Delta E_g}{\Delta E_k} \frac{B_k(E') B_g(E)}{\Delta E_g}$$
$$+ \sigma_{s,k \to k}^{(l)} \frac{\Delta E_k}{\Delta E_k} \delta(E' - E) B_k(E) \ , \tag{83}$$

$$= \sum_{k=1}^{N} \sum_{g=1}^{N} \sigma_{s,g \to k}^{(l)} \frac{\Delta E_g}{\Delta E_k} \circledB_{k,g}(E', E) \ ,$$

$$= \sum_{k=1}^{N} \sum_{g=1}^{N} \sigma_{s,k \to g}^{\dagger(l)} \circledB_{k,g}(E', E) \ , \tag{84}$$

where

$$\sigma_{s,k \to g}^{\dagger(l)} = \sigma_{s,g \to k}^{(l)} \frac{\Delta E_g}{\Delta E_k} \ . \tag{85}$$

Note that the step from Eq. (82) to Eq. (83) is justified by the fact that

$$\int_{E_{N+1/2}}^{E_{1/2}} \delta(E' - E) B_k(E) \psi^\dagger(E') \, dE'$$
$$= \int_{E_{N+1/2}}^{E_{1/2}} \delta(E - E') B_k(E') \psi^\dagger(E') \, dE' \ . \tag{86}$$

It follows from Eqs. (30) and (84) that the forward and adjoint algorithms for sampling smooth-component Boltzmann scattering differ only in that the expansion coefficients for the forward kernel are used in the forward algorithm whereas the expansion coefficients for the adjoint kernel are used in the adjoint algorithm. It can also be seen from Eq. (85) that the adjoint kernel expansion coefficients can be trivially calculated from the forward kernel coefficients. Note that Eq. (85) is consistent with Eq. (73).

To demonstrate the only significant differences between the forward and adjoint solution algorithms, we first consider the adjoint continuous slowing down terms:

$$\left[\frac{\partial}{\partial E} (\tilde{S} \psi) \right]^\dagger = -\frac{\partial}{\partial E} (\tilde{S} \psi^\dagger) + \frac{\partial \tilde{S}}{\partial E} \psi^\dagger \ . \tag{87}$$

The first operator on the right side of Eq. (87) simply causes particles to speed up at the same rate that the forward operator causes them to slow down. If $\partial \tilde{S}/\partial E$ is positive, the second operator on the right side of Eq. (87) is analogous to a particle production operator with the energy derivative of the restricted stopping power playing the role of the production cross section, and if $\partial \tilde{S}/\partial E$ is negative, this operator is analogous to a particle absorption operator with the energy derivative of the restricted stopping power playing the role of the absorption cross section. Thus, if $\partial \tilde{S}/\partial E$ is positive, particles will be produced, and if $\partial \tilde{S}/\partial E$ is negative, particles will be removed. Note that the particles that are produced will have the same energy and direction as the particle that produces them. Rather than actually remove or produce particles in the Monte Carlo

simulation process, we choose to appropriately reduce or increase the weight of the primary particle. Thus, from a Monte Carlo viewpoint, one can think of the adjoint continuous slowing down operator as continuously speeding particles up at a rate equal to the restricted stopping power, while simultaneously changing their weights in proportion to the energy derivative of the restricted stopping power. The weight-change factor associated with this process has been given previously by Halbleib and Morel.[17] For completeness, we derive it here for the piecewise-constant form of the restricted stopping power assumed in Eq. (63).

The derivation is begun by assuming that a normally incident monoenergetic pencil-beam of adjoint particles at energy E_0 enters a homogeneous slab of material at position $x = 0$ at the rate of one particle per second, as shown in Fig. 1. It is further assumed that within the slab, $\tilde{\sigma}_t(E) \equiv 0$ and $\tilde{\alpha}(E) \equiv 0$. Let $\psi^\dagger(x,E)\,dE$ represent the number of adjoint particles at energy E reaching the point x per unit time. Following Eq. (63), we can write an equation for this beam-flux quantity as

$$\frac{\partial \psi^\dagger}{\partial x} + \frac{\partial}{\partial E}(\tilde{S}\psi^\dagger) = \frac{\partial \tilde{S}}{\partial E}\psi^\dagger , \tag{88}$$

with the initial condition

$$\psi^\dagger(0,E) = \delta(E - E_0) . \tag{89}$$

If $\partial \tilde{S}/\partial E$ is assumed to be identically zero in Eq. (88), the adjoint particles continually speed up at a rate equal to the stopping power. For this case, the solution to Eq. (88) is

$$\psi^\dagger(x,E) = \delta[E - E(x)] , \tag{90}$$

where $E(x)$ is implicitly defined by the following equation:

$$x = \int_{E_0}^{E(x)} S(E)^{-1}\,dE . \tag{91}$$
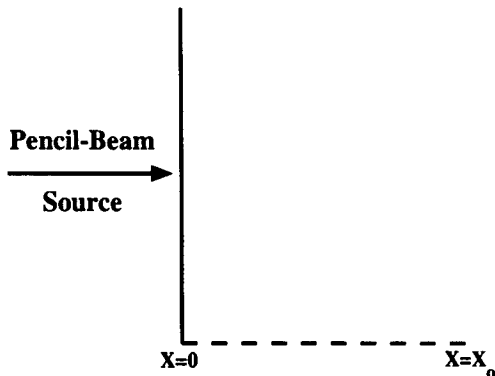

Pencil-Beam

Source

X=0   X=X$_0$

Fig. 1. Geometry for adjoint slowing down weight-factor derivation.

As previously noted, the operator on the right side of Eq. (88) either causes primary particles to be absorbed or generates secondary particles at the same energy as the particles that produce them. Taking this property into account, it follows from Eq. (90) that the general solution to Eq. (88) must have the following form:

$$\psi^\dagger(x,E) = c(x)\delta[E - E(x)] . \tag{92}$$

Substituting from Eq. (92) into Eq. (88) and then integrating Eq. (88) over all energies, we obtain

$$\frac{\partial}{\partial x}c(x) = S'(x)c(x) , \tag{93}$$

where

$$S' = \frac{\partial \tilde{S}}{\partial E} . \tag{94}$$

The solution to Eq. (93) is

$$c(x) = \exp\left[\int_0^x S'(x')\,dx'\right] . \tag{95}$$

From Eq. (91), it follows that

$$dx = S(E)^{-1}\,dE . \tag{96}$$

Substituting from Eq. (96) into Eq. (95), we get

$$c(x) = \exp\left[\int_{E_0}^{E(x)} \frac{S'}{S}\,dE\right] ,$$
$$= \exp\left(\log_e\{S[E(x)]\} - \log_e\{S[E(0)]\}\right) ,$$
$$= \frac{S[E(x)]}{S[E(0)]} . \tag{97}$$

Since $c(x)$ represents the total number of particles in the beam reaching the point x per unit time, it follows that a Monte Carlo particle should change its weight in moving from $x = 0$ to $x = x_0$ by a multiplicative factor equal to $c(x_0)$.

Because of the piecewise-constant dependence of our approximate restricted stopping power function, it follows that the restricted stopping power of an adjoint particle transporting according to Eq. (63) will only change when the particle speeds up across a group boundary. Thus, it is only at this point that its weight is changed, and the multiplicative factor by which it changes follows from Eq. (97):

$$W_c = \frac{S_{g-1}}{S_g} , \tag{98}$$

where g denotes the group that the particle leaves and $g - 1$ denotes the group that the particle enters.

The continuous speeding up of adjoint particles leads to the following expression for the adjoint distance-to-energy boundary:

$$D_e^\dagger = \frac{E_{g-1/2} - E_p}{S_g} . \tag{99}$$

Furthermore, whenever an adjoint particle speeds up across a group boundary, its weight is multiplied by the factor defined by Eq. (98). This only occurs when the distance-to-collision exceeds the distance-to-energy boundary.

Thus, the only significant difference between our forward and adjoint Monte Carlo solution algorithms arises from a unique particle weight change associated with the adjoint algorithm that only occurs when a particle moves into a new energy group through the action of the adjoint continuous slowing down operator.

VII. CROSS-SECTION DATA GENERATION

Our algorithm requires restricted stopping powers and momentum transfers for each group, and smooth-component multigroup Legendre transfer cross sections. We have generated such data for coupled electron-photon transport calculations using a slightly modified version of the CEPXS code.[18] The CEPXS code generates multigroup coupled electron-photon cross-section data for the ONELD discrete ordinates code[19,20] and models essentially the same physics as the Integrated TIGER Series[21](ITS) family of coupled electron-photon Monte Carlo codes. The equation solved with CEPXS/ONELD consists of the standard Boltzmann equation together with the continuous slowing down operator, whereas the equation that we solve consists of the Boltzmann equation together with both the continuous slowing down and continuous-scattering operators. Thus, to obtain the data required for our Monte Carlo method, we added a capability to CEPXS for generating restricted momentum transfers.

The algorithm that we use to generate the momentum transfers is called the moment-based angular Fokker-Planck decomposition technique.[4] Given the Legendre moments of the cross section for scattering from group g to group g, the moment-based scheme produces a similar set of Legendre moments representing the smooth component of that cross section together with a restricted momentum transfer for group g.

As previously stated, CEPXS generates restricted stopping powers for each group. However, in CEPXS these restricted stopping powers are imbedded in the multigroup Legendre transfer matrices because a multigroup Legendre cross-section representation[22] is used for the continuous slowing down operator. We modified the code to eliminate the contributions from the continuous slowing down operator to the multigroup transfer matrices and to explicitly place the restricted stopping powers in the cross-section output file for access by our Monte Carlo code.

In the standard CEPXS algorithm, the cross sections for transferring from electron group g to electron group $g + 1$ are completely determined by the contributions from the diamond difference continuous slowing down operator. When these contributions are eliminated, these transfer cross sections are identically

zero. This means that there will be no contribution to the mean-squared stopping power from transfers between adjacent groups, even though a significant contribution to the mean-squared stopping power is expected to come from such transfers. In the Fokker-Planck limit, the mean-squared stopping power determines the amount of straggling experienced by the particles.[3] While initially testing our scheme, we noticed that solutions for the electron energy spectra sometimes exhibited a lack of straggling effects, i.e., a lack of spectral broadening. Ideally, one would like to define the cross sections for transferring from electron group g to electron group $g + 1$ in such a way as to ensure the correct mean-square stopping power. This is done by making the following definition:

$$\sigma_{g \to g+1}(\mu_0) = \frac{\gamma(E_g)}{(E_g - E_{g+1})^2} \frac{1}{2\pi} \delta(\mu_0 - 1) , \quad (100)$$

where $\gamma(E_g)$ denotes the restricted mean-square stopping power at energy E_g, and g takes on all values associated with the electron groups. Unfortunately, accurate electron mean-square stopping power data are not readily available, so as a first step toward a more accurate and formal definition, we simply make the following ad hoc definition for the transfer cross section from group g to group $g + 1$:

$$\sigma_{g \to g+1}(\mu_0) = \sigma_s(E_g \to E_{g+1})(E_{g+1/2} - E_{g+3/2})$$
$$\times \frac{1}{2\pi} \delta(\mu_0 - 1) , \quad (101)$$

where $\sigma_s(E' \to E)$ denotes the electron macroscopic scattering cross section averaged over all angles of scatter. The stopping power associated with the transfer from group g to group $g + 1$ is

$$\beta_{g \to g+1} = \sigma^{(0)}_{g \to g+1}(E_g - E_{g+1}) . \quad (102)$$

The use of the delta-function angular distribution in Eqs. (100) and (101) is in accordance with the use of a continuous slowing down approximation (CSDA) for the transfers from group g to group $g + 1$. To ensure that the total stopping power is correct, the stopping power defined by Eq. (102) is subtracted from the restricted stopping power normally calculated by CEPXS.

The restricted momentum transfers and stopping powers calculated with our modified version of CEPXS are written to the cross-section output file in a location normally reserved for reaction rate cross sections. This allows us to access the momentum transfers and restricted stopping powers without modifying the standard cross-section file formats[19] available from CEPXS. The restricted momentum transfers and restricted stopping powers are identically zero for all photon groups.

VII.A. Reaction Rates

Reaction rates are usually calculated in multigroup Monte Carlo codes by first calculating the group-dependent particle fluxes and then folding these fluxes

with the appropriate reaction cross sections. For the most part, this same basic approach can be used with our BFP multigroup scheme, but the presence of the continuous slowing down operator and the piecewise-constant energy dependence of our cross sections necessitates the calculation of certain quantities, in addition to the standard multigroup scalar fluxes, to generate certain types of reaction rates. For instance, when particles slow down below the lowest energy in the last group (the so-called cutoff energy) they are considered to be "absorbed" by the transport medium. Such absorption events clearly contribute to certain reaction rates such as energy deposition and charge deposition in the transport medium. However, because particles are absorbed precisely when they reach the cutoff energy, the effective cross section for absorption corresponds to a delta-function in energy, i.e.,

$$\sigma_{ea}(E) = \delta(E - E_{N+1/2}) , \qquad (103)$$

where σ_{ea} denotes the effective absorption cross section and $E_{N+1/2}$ denotes the lowest energy in the last group (the cutoff energy). The reaction rate for such a cross section is the folding of an infinitesimal flux (the flux due to particles with energies exactly equal to $E_{N+1/2}$) and an infinite cross section (the delta-function cross section). Thus, the effective absorption rate due to the energy cutoff cannot be calculated purely in terms of the average flux normally calculated for the last group. Rather, one must explicitly calculate this effective absorption rate and appropriately weight it to obtain the contribution for a given reaction rate. For instance, the rate at which energy is deposited by the particles slowing down below the cutoff energy is equal to the rate at which particles fall below the cutoff energy multiplied by the cutoff energy. Similarly, the rate at which charge is deposited by the particles slowing down below the cutoff energy is equal to the rate at which particles slow down below the cutoff energy multiplied by the charge per particle. We stress that contributions to reaction rates from particles that scatter below the cutoff energy rather than slow down below the cutoff energy are calculated using the standard group-averaged scalar fluxes together with a set of group-dependent reaction rate cross-section values.

The energy-deposition cross sections generated by the CEPXS code are not rigorously correct for our algorithm. This follows from the fact that the energy-deposition rate is not a simple reaction rate, but rather an energy-weighted reaction rate. For instance, to calculate the net rate at which particles deposit energy per unit volume in the transport medium, we first subtract the removal term in Eq. (39) from the sum of the in-scatter term and the CSDA term in Eq. (39). Next, we multiply the resulting expression by E and integrate that expression over all directions and energies. A standard reaction rate would not include the multiplication by E. Finally, we algebraically manipulate the resulting expression into the following form:

$$D_e = \sum_{g=1}^{N} \langle E \rangle_g \sigma_{t,g} \Phi_g - \sum_{g=1}^{N} E_g \sum_{k=1}^{g} \sigma_{s,k \to g}^{(0)} \Phi_k$$
$$+ \sum_{g=1}^{N} S_g \Phi_g + E_{N+1/2} S_{N+1/2} \phi(E_{N+1/2}) , \qquad (104)$$

where

D_e = energy deposition rate (energy/volume-time)

E_g = midpoint energy for group g

Φ_g = multigroup scalar flux:

$$\Phi_g = \int_{E_{g+1/2}}^{E_{g-1/2}} \phi(E) \, dE \qquad (105)$$

$\langle E \rangle_g$ = flux-weighted average energy for group g:

$$\langle E \rangle_g = \frac{1}{\Phi_g} \int_{E_{g+1/2}}^{E_{g-1/2}} \Phi(E) E \, dE \qquad (106)$$

$S_{N+1/2} \phi(E_{N+1/2})$

= number of particles per unit time per unit volume slowing down below the cutoff energy.

As previously discussed, this latter quantity must be calculated in addition to the standard multigroup fluxes in order to properly calculate charge and energy deposition with our algorithm. By manipulating Eq. (104), we can define a multigroup cross section for energy deposition as follows:

$$E_d = \sum_{g=1}^{G} \sigma_g^e \Phi_g , \qquad (107)$$

where

$$\sigma_g^e = \langle E \rangle_g \sigma_{t,g} - E_g \sum_{k=1}^{g} \sigma_{s,k \to g}^{(0)} + S_g , \qquad (108)$$

and where σ_g^e denotes the energy-deposition cross section for group g. The standard multigroup energy-deposition cross section generated by CEPXS can be obtained simply by replacing $\langle E \rangle_g$ in Eq. (108) with E_g. If the flux is constant within group g, then $\langle E \rangle_g = E_g$, and the two cross-section expressions become equivalent. Thus, the CEPXS energy-deposition cross section will be accurate as long as the flux varies slowly within each group. Since it is desirable to avoid the expense associated with calculating flux-averaged energies in addition to the group-integrated fluxes, we have chosen to use the default CEPXS energy-deposition cross sections. Computational testing indicates that this is an excellent approximation. We stress that the term in Eq. (104) proportional to $S_{N+1/2} \phi(E_{N+1/2})$ does not appear in a standard multigroup approximation and arises from both the CSDA operator and the continuous-energy aspect of our Monte Carlo algorithm.

VIII. COMPUTATIONAL RESULTS

In this section, we computationally compare our hybrid multigroup/continuous-energy BFP (MGBFP) algorithm with the standard condensed history algorithm of the coupled electron-photon transport code, CYLTRAN (Ref. 21). In addition, we demonstrate the validity of our adjoint MGBFP algorithm. The CYLTRAN code is a well-known production code that is in routine use in the radiation effects, radiation shielding, and medical physics communities. As previously discussed, we use the CEPXS code[18] to generate the coupled electron-photon cross-section data for our MGBFP algorithm. The basic cross-section data used by the CEPXS and CYLTRAN codes are nearly identical, so any significant differences between the MGBFP and CYLTRAN solutions should be due to algorithmic differences rather than differences in basic cross-section data. We have performed two sets of calculations: a forward and an adjoint set.

Each calculation in the forward set was performed both with our MGBFP method and the condensed history method. All of the forward calculations correspond to a pencil-beam source of monoenergetic electrons incident upon a cylinder of tungsten, as shown in Fig. 2. Note from Fig. 2 that the radius of the cylinder is always equal to its length. We chose a pencil-beam source to strongly test the use of discrete-scattering distributions in our Monte Carlo algorithm. Calculations were performed for three beam energies: 0.1, 1.0, and 10.0 MeV, having cutoff energies of 0.01, 0.01, and 0.1 MeV, respectively. For each beam energy, calculations were performed for two axial lengths: one-fifth and one-half the range of an electron at the beam energy. Each of these six basic problems is assigned a number in Table IV. Fifty electron groups and 50 photon groups were used in conjunction with P_{15} Legendre cross-section expansions in all of the calculations. The electron groups were all of uniform width. The photon groups had widths that logarithmically decreased with decreas-
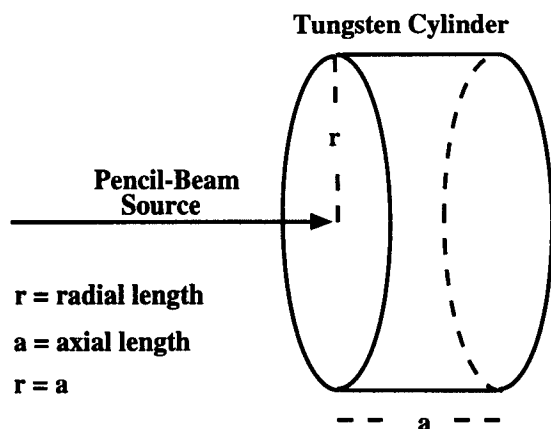
TABLE IV
Numbering for First Set of Calculations

Problem Number	Source Energy (MeV)	Cutoff Energy (MeV)	Axial Thickness (Range Fraction)
1	0.1	0.01	0.2
2	0.1	0.01	0.5
3	1.0	0.01	0.2
4	1.0	0.01	0.5
5	10.0	0.1	0.2
6	10.0	0.1	0.5

ing group energy. The highest and lowest energies in the electron and photon group structures were identical, and the lowest energy was equal to the cutoff energy. The midpoint energy of the first electron group was equal to the source energy, and the monoenergetic electron sources were modeled with a flat (uniformly distributed) source in the first group.

The radially averaged energy deposition profiles for problems 1 through 6 are compared in Figs. 3 through 8. The agreement between the MGBFP and CYLTRAN profiles is generally good. The total energy deposition values for all problems are compared in Table V. The agreement between the MGBFP and CYLTRAN results is similarly good with the largest disagreement on the order of 4%. The axially transmitted, radially transmitted, and reflected electron number fractions for all problems are compared in Table VI, and the analogous photon number fractions are compared in Table VII.

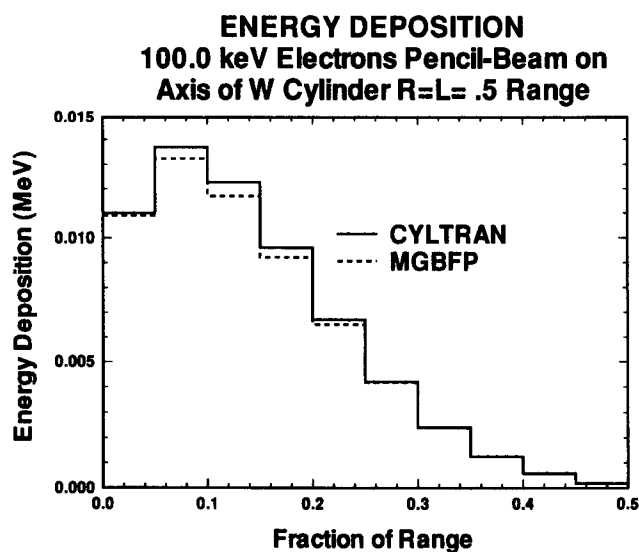Fig. 2. Geometry for set of forward test calculations.

Fig. 3. Comparison of energy deposition profiles for problem 1. Each datum used to construct this plot exhibited a relative standard percent statistical deviation of <1%.
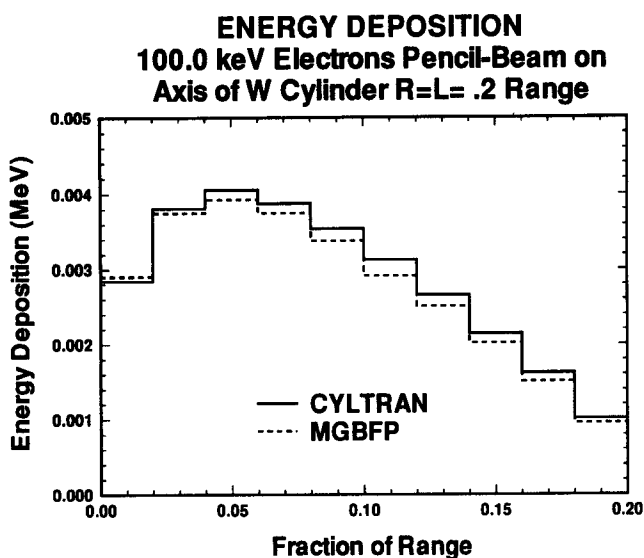
Fig. 4. Comparison of energy deposition profiles for problem 2. Each datum used to construct this plot exhibited a relative standard percent statistical deviation of <1%.

Fig. 6. Comparison of energy deposition profiles for problem 4. Each datum used to construct this plot exhibited a relative standard percent statistical deviation of <1%.

Fig. 5. Comparison of energy deposition profiles for problem 3. Each datum used to construct this plot exhibited a relative standard percent statistical deviation of <1%.
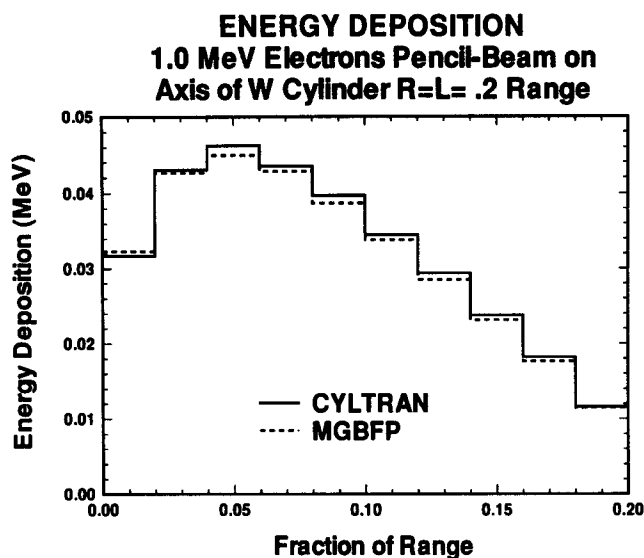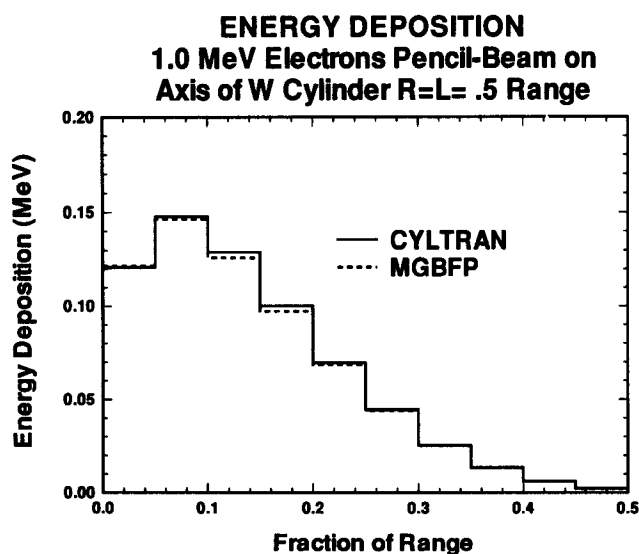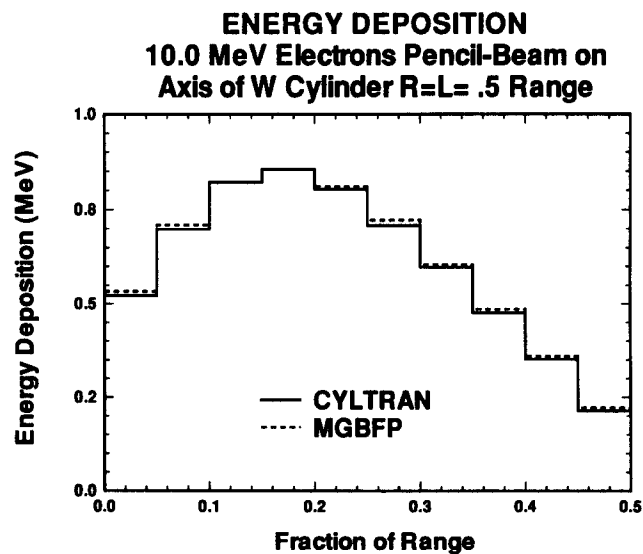

Fig. 7. Comparison of energy deposition profiles for problem 5. Each datum used to construct this plot exhibited a relative standard percent statistical deviation of <1%.

The agreement between the MGBFP and CYLTRAN results is good on the whole with a maximum disagreement of ~8% for the electron fractions and ~7% for the photon fractions. The axially transmitted electron and continuum photon spectra for problem 3 are compared in Figs. 9 and 10, respectively. The agreement between the MGBFP and CYLTRAN electron spectra is generally good but shows evidence of slightly different amounts of straggling in the two algorithms. This is to be expected since the mean-square stopping power, which largely determines the electron straggling, is at

present only crudely preserved in the MGBFP algorithm. However, if accurate mean-square stopping powers could be obtained, accurate straggling in the MGBFP algorithm could be achieved via Eq. (100).[b] The agreement between the MGBFP and CYLTRAN photon spectra is quite good. Overall, the agreement between

---

[b]It is conceivable that such mean-square stopping powers could be extracted from the straggling model in the ITS codes. We intend to investigate this possibility in the near future.

ENERGY DEPOSITION
10.0 MeV Electrons Pencil-Beam on
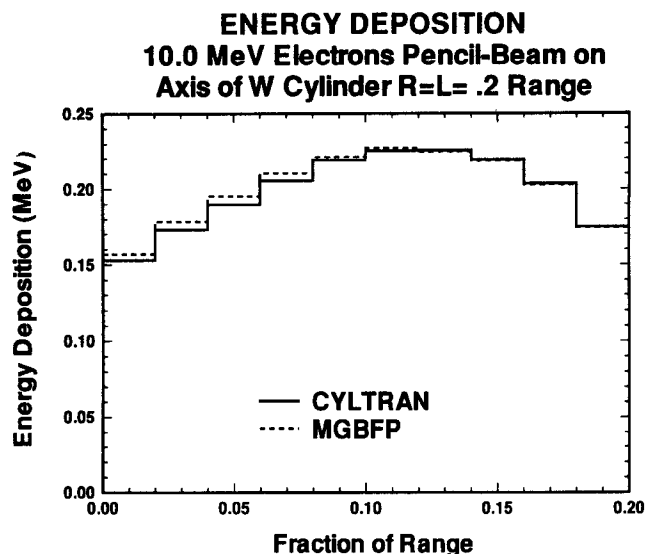### Axis of W Cylinder R=L= .2 Range

Fig. 8. Comparison of energy deposition profiles for problem 6. Each datum used to construct this plot exhibited a relative standard percent statistical deviation of <1%.

TABLE V

Comparison of Total Energy Deposition (MeV)

Problem	CYLTRAN	MGBFP	Percent Difference[a]
1	2.87×10^{-2} (0)[b]	2.76×10^{-2} (0)	−3.8
2	6.19×10^{-2} (0)	6.02×10^{-2} (0)	−2.7
3	3.22×10^{-1} (0)	3.16×10^{-1} (0)	−1.8
4	6.59×10^{-1} (0)	6.50×10^{-1} (0)	−1.4
5	1.99 (0)	2.01 (0)	1.0
6	6.05 (0)	6.12 (0)	1.2

[a]Relative to the CYLTRAN solution.

[b]The integer in parenthesis following each datum represents the standard relative percent statistical deviation for that datum rounded to the nearest integer.

the MGBFP and CYLTRAN algorithms is well within acceptable bounds for engineering applications.

The second set of calculations consists of ten adjoint response calculations. Each response consists of the radially integrated energy deposition in one of ten uniform axial zones spanning a cylinder of tungsten. The cylinder is illustrated in Fig. 11. The left axial face of the cylinder is spanned by a spatially uniform cosine-law disk source of 10.0-MeV electrons. The axial length of the cylinder is equal to one-fifth the range of a 10.0-MeV electron in tungsten, and the radius of the cylinder is equal to its axial length. The adjoint MGBFP results and forward CYLTRAN results for the energy deposited in the cylinder are compared in Fig. 12. The agreement between the forward and adjoint profiles is excellent. Since our approximate forward BFP equation is rigorously adjoint to our approximate adjoint

TABLE VI

Comparison of Transmitted and Reflected Electron Number Fractions

Problem	CYLTRAN	MGBFP	Percent Difference[a]
Reflected			
1	3.90×10^{-1} (0)[b]	4.05×10^{-1} (0)	3.8
2	4.85×10^{-1} (0)	5.00×10^{-1} (0)	3.1
3	3.44×10^{-1} (0)	3.47×10^{-1} (1)	0.9
4	4.49×10^{-1} (0)	4.53×10^{-1} (0)	0.9
5	3.74×10^{-2} (1)	3.98×10^{-2} (2)	6.4
6	1.19×10^{-1} (1)	1.19×10^{-1} (1)	0.0
Axially Transmitted			
1	2.45×10^{-1} (0)	2.34×10^{-1} (0)	−4.5
2	4.28×10^{-1} (1)	3.96×10^{-1} (1)	−7.5
3	2.69×10^{-1} (0)	2.71×10^{-1} (1)	0.7
4	4.36×10^{-3} (1)	4.79×10^{-3} (1)	9.0
5	7.34×10^{-1} (0)	7.36×10^{-1} (0)	0.3
6	1.82×10^{-1} (1)	1.86×10^{-1} (1)	2.2
Radially Transmitted			
1	2.91×10^{-1} (0)	2.89×10^{-1} (0)	−0.7
2	4.33×10^{-1} (2)	4.23×10^{-1} (1)	−2.3
3	3.21×10^{-1} (0)	3.23×10^{-1} (1)	0.6
4	4.49×10^{-3} (0)	4.74×10^{-3} (0)	5.6
5	2.24×10^{-1} (0)	2.22×10^{-1} (1)	−0.9
6	1.03×10^{-1} (1)	9.94×10^{-2} (1)	−3.5

[a]Relative to the CYLTRAN solution.

[b]The integer in parenthesis following each datum represents the standard relative percent statistical deviation for that datum rounded to the nearest integer.

TRANSMITTED ELECTRON SPECTRUM
1.0 MeV Electrons Pencil-Beam on
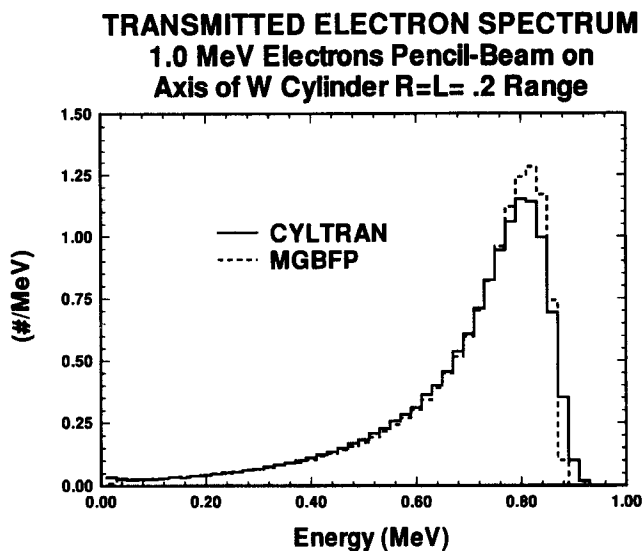### Axis of W Cylinder R=L= .2 Range

Fig. 9. Comparison of axially transmitted electron spectra for problem 3. Each datum used to construct this plot exhibited a relative standard percent statistical deviation of <4%.

TABLE VII

Comparison of Transmitted and Reflected Photon
Number Fractions

Problem	CYLTRAN	MGBFP	Percent Difference[a]
		Reflected	
1	2.57×10^{-3} $(2)^{b}$	2.46×10^{-3} (2)	-4.3
2	5.12×10^{-3} (1)	5.16×10^{-3} (1)	0.8
3	2.98×10^{-2} (1)	2.89×10^{-2} (2)	-3.0
4	6.84×10^{-2} (1)	6.53×10^{-2} (0)	-4.5
5	2.67×10^{-2} (0)	2.55×10^{-2} (2)	-4.5
6	2.11×10^{-1} (1)	2.00×10^{-1} (1)	-5.2
		Axially Transmitted	
1	2.63×10^{-3} (2)	2.46×10^{-3} (2)	-6.5
2	2.34×10^{-3} (2)	2.31×10^{-3} (1)	-1.3
3	4.55×10^{-2} (2)	4.50×10^{-2} (2)	-1.1
4	3.76×10^{-2} (1)	3.58×10^{-2} (1)	-4.8
5	7.23×10^{-1} (0)	7.28×10^{-1} (0)	0.7
6	9.55×10^{-1} (0)	9.64×10^{-1} (0)	0.9
		Radially Transmitted	
1	4.52×10^{-3} (1)	4.38×10^{-3} (1)	-3.1
2	4.41×10^{-3} (1)	4.40×10^{-3} (1)	-0.2
3	6.31×10^{-2} (0)	6.23×10^{-2} (1)	-1.3
4	6.17×10^{-2} (1)	5.75×10^{-2} (0)	-6.8
5	1.98×10^{-1} (0)	1.96×10^{-1} (1)	-1.0
6	6.85×10^{-1} (0)	6.56×10^{-1} (0)	-4.2

[a]Relative to the CYLTRAN solution.

[b]The integer in parenthesis following each datum represents the standard relative percent statistical deviation for that datum rounded to the nearest integer.

equation, the forward and adjoint solutions should become identical in the limit as the number of particle histories generated in each calculation is increased without bound.

It is not our purpose here to describe the various uses of our adjoint algorithm or the detailed calculational procedures associated with those uses. Rather, we simply seek to demonstrate that our algorithm is valid. The uses for adjoint electron transport methods and adjoint coupled electron-photon transport methods are discussed in Refs. 17 and 23, respectively. The reader is reminded that the inner product associated with our adjoint MGBFP algorithm is identical to the continuous-energy inner product used in Ref. 17, but it differs from the standard multigroup inner product used in Ref. 23. This lack of equivalence is a technicality that does not diminish the overall applicability of Ref. 23 to our MGBFP algorithm. As illustrated by Eqs. (78) and (79), one need only slightly modify the adjoint sources consistent with the standard multigroup

**TRANSMITTED PHOTON
SPECTRUM (CONTINUUM)
1.0 MeV Electrons Pencil-Beam on
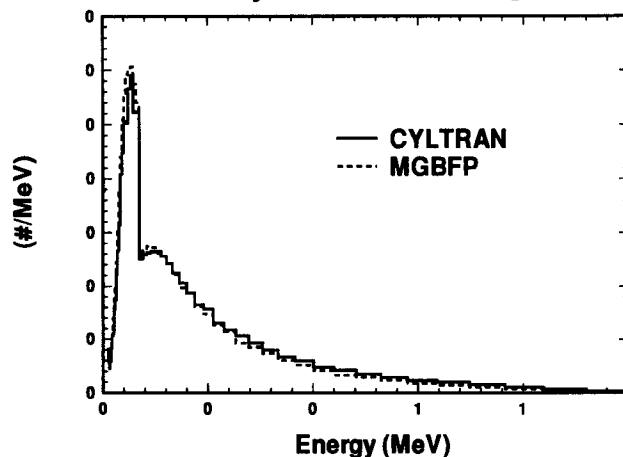Axis of W Cylinder R=L= .2 Range**

Fig. 10. Comparison of axially transmitted photon spectra for problem 3. Each datum used to construct this plot exhibited a relative standard percent statistical deviation of <5%.
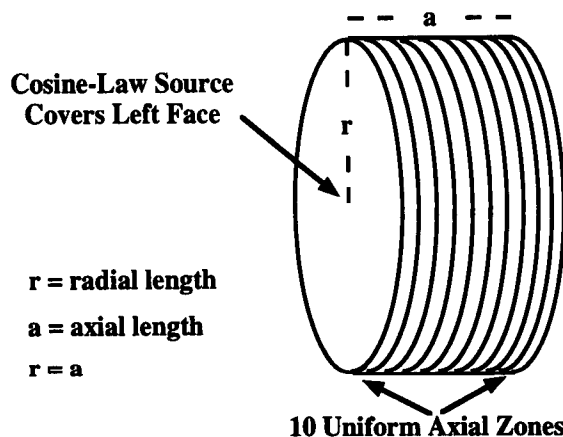
Tungsten Cylinder

Fig. 11. Geometry for set of forward/adjoint test calculations.

inner product to obtain the sources consistent with our multigroup MGBFP inner product.

IX. SUMMARY AND CONCLUSIONS

The MGBFP algorithm that we have developed is a generalization of the standard neutral-particle multigroup Monte Carlo method. To a certain extent, our

Cosine-law Disk Source; 10 MeV Electrons
Pencil-Beam on Axis of W Cylinder
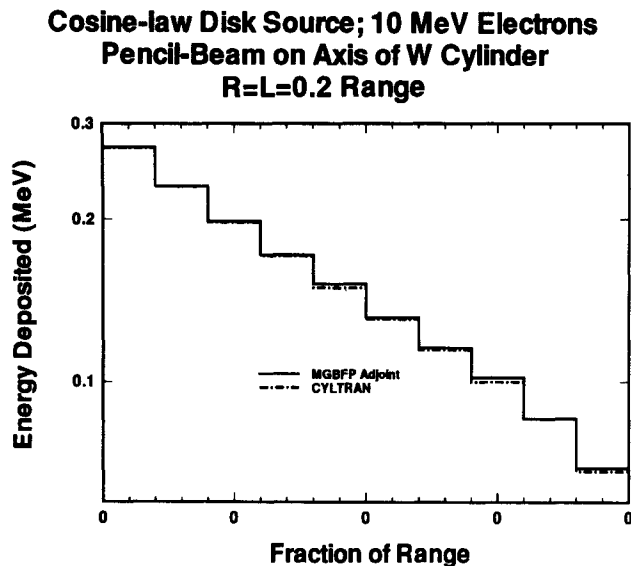## R=L=0.2 Range

Fig. 12. Comparison of forward and adjoint energy deposition profiles.

algorithm also represents a new form of condensed history algorithm. However, our algorithm uses an exponential distribution of path lengths between condensed collisions rather than a fixed path length between such collisions. Here, we use the words "condensed collision" to denote any event in which the energy or direction of a Monte Carlo particle is changed to account for the effect of many real collisions. By using an exponential distribution of path lengths in conjunction with a hybrid multigroup/continuous-energy approximation, we obtain an algorithm that is very similar to the standard neutral-particle multigroup Monte Carlo algorithm. Consequently, our MGBFP algorithm can be easily implemented in a standard neutral-particle multigroup Monte Carlo code. Our MGBFP algorithm also includes an adjoint algorithm. This adjoint algorithm is similar to a standard neutral-particle multigroup adjoint algorithm in that it uses the same basic cross-section data as the forward algorithm and can be implemented in a code by trivially modifying the forward algorithm.

Our MGBFP algorithm has been implemented in a Monte Carlo code system that combines the physics, input/output, and geometry capabilities of version 3.0 of the ITS code system,[21] the coupled electron-photon multigroup cross-section generation capability of the CEPXS code,[18-20] and the discrete-scattering distribution generation capability of a module originally taken from the MORSE code[7] and modified by Sloan.[14] Our computational results indicate that for coupled electron-photon transport calculations, our MGBFP method is comparable to a standard condensed history method.

In the future, we will test our MGBFP method for other types of charged-particle calculations. Some testing has already been done for coupled neutron-proton transport.[24]

REFERENCES

1. K. PRZYBYLSKI and J. LIGOU, "Numerical Analysis of the Boltzmann Equation Including Fokker-Planck Terms," *Nucl. Sci. Eng.*, **81**, 92 (1982).

2. M. CARO and J. LIGOU, "Treatment of Scattering Anisotropy of Neutrons Through the Boltzmann-Fokker-Planck Equation," *Nucl. Sci. Eng.*, **83**, 242 (1983).

3. J. E. MOREL, "Fokker-Planck Calculations Using Standard Discrete Ordinates Transport Codes," *Nucl. Sci. Eng.*, **79**, 340 (1981).

4. M. LANDESMAN and J. E. MOREL, "Angular Fokker-Planck Decomposition and Representation Techniques," *Nucl. Sci. Eng.*, **103**, 1 (1989).

5. M. J. BERGER, "Monte Carlo Calculation of the Penetration and Diffusion of Fast Charged Particles," *Methods in Computational Physics*, Vol. 1, p. 135, Academic Press, New York (1963).

6. J. S. ZIEGLER, J. P. BIERSACK, and U. LITTMARK, *Stopping and Ranges of Ions In Matter*, Pergamon Press, New York (1985).

7. M. B. EMMETT, "The MORSE Monte Carlo Radiation Transport Code System," ORNL-4972, Oak Ridge National Laboratory (1975).

8. J. A. HALBLEIB, Sr., "Continuous-Energy Adjoint Monte Carlo Theory of Coupled Continuum/Discrete Radiation Transport," *Nucl. Sci. Eng.*, **80**, 162 (1982).

9. *Handbook of Mathematical Functions*, M. ABRAMOWITZ and I. STEGUN, Eds., Dover Publications, Inc. (1965).

10. G. BELL and S. GLASSTONE, *Nuclear Reactor Theory*, Van Nostrand Reinhold Company, New York (1968).

11. A. H. STROUD and D. SECREST, *Gaussian Quadrature Formulas*, Prentice-Hall, New Jersey (1966).

12. K. D. LATHROP, "Anisotropic Scattering Approximations in the Monoenergetic Boltzmann Equation," *Nucl. Sci. Eng.*, **21**, 498 (1965).

13. J. E. MOREL, "On the Validity of the Extended Transport Cross-Section Correction for Low-Eenrgy Electron Transport," *Nucl. Sci. Eng.*, **71**, 64 (1979).

14. D. P. SLOAN, "A New Multigroup Monte Carlo Scattering Algorithm Suitable for Neutral and Charged-Particle

Boltzmann and Fokker-Planck Calculations," SAND83-7094, Sandia National Laboratories (May 1983).

15. J. SPANIER and E. M. GELBARD, *Monte Carlo Principles and Neutron Transport Problems*, Addison-Wesley Publishing Co., Reading, Massachusetts (1969).

16. F. R. GANTMACHER, *The Theory of Matrices*, Vol. I, Chelsea Publishing Co., New York (1959).

17. J. A. HALBLEIB and J. E. MOREL, "Adjoint Monte Carlo Electron Transport in the Continuous Slowing-Down Approximation," *J. Comp. Phys.*, **34**, 211 (1980).

18. L. J. LORENCE, Jr., J. E. MOREL, and G. D. VALDEZ, "Physics Guide to CEPXS: A Multigroup Coupled Electron-Photon Cross-Section Generating Code," SAND89-1685, Sandia National Laboratories (1989).

19. L. J. LORENCE, Jr., J. E. MOREL, and G. D. VALDEZ, "User's Guide to CEPXS/ONELD: A One-Dimensional Coupled Electron-Photon Discrete Ordinates Code Package," SAND89-1661, Sandia National Laboratories (1989).

20. L. J. LORENCE, Jr., J. E. MOREL, and G. D. VALDEZ, "Results Guide to CEPXS/ONELD: A One-Dimensional Coupled Electron-Photon Discrete Ordinates Code Package," SAND89-2211, Sandia National Laboratories (1990).

21. J. A. HALBLEIB, R. P. KENSEK, G. D. VALDEZ, S. M. SELTZER, and M. J. BERGER, "ITS: The Integrated TIGER Series of Coupled Electron/Photon Monte Carlo Transport Codes—Version 3.0," *IEEE Trans. Nucl. Sci.*, **39**, 1025 (1992).

22. J. E. MOREL, "Multigroup Legendre Coefficients for the Diamond Difference Continuous Slowing Down Operator," *Nucl. Sci. Eng.*, **91**, 324 (1985).

23. C. R. DRUMM, W. C. FAN, and J. H. RENKEN, "Forward and Adjoint Methods and Applications for Deterministic Electron-Photon Transport," *Nucl. Sci. Eng.*, **108**, 16 (1991).

24. W. L. FILIPPONE, R. C. LITTLE, J. E. MOREL, R. E. MacFARLANE, and P. G. YOUNG, "Coupled Proton/Neutron Transport Calculations Using the S_N and Monte Carlo Methods," *Proc. Int. Topl. Mtg. Advances in Mathematics, Computations, and Reactor Physics*, Pittsburgh, Pennsylvania, April 28–May 2, 1991, Vol. 1, Sec. 2.1, p. 1-1, American Nuclear Society (1991).